Dynamical interference structures in fully coupled bound-bound state quantum wave-packet dynamics

Niklas Gador and Bo Zhang
Department of Physics, Royal Institute of Technology, AlbaNova University Center, SE-106 91 Stockholm, Sweden

Hans O. Karlsson
Department of Quantum Chemistry, Uppsala University, Box 518, SE-751 20 Uppsala, Sweden

Tony Hansson*
Department of Physics, Stockholm University, AlbaNova University Center, SE-106 91 Stockholm, Sweden
(Received 18 May 2004; published 28 September 2004)

The quantum wave-packet dynamics in a bound-bound state system at intermediate coupling strength, the A and b states in the Rb_2 molecule coupled by spin-orbit interaction, was studied by ultrafast pump-probe molecular beam spectrocopy and quantum dynamical calculations. It was shown that even at elevated molecular temperatures the experimentally observed traces are characterized by dynamical interference structures of mesobatic, i.e., diabatic-adiabatic hybrid, kind. Two types of mesobatic motion were discerned: bistable, which occurs in both bound-unbound and bound-bound systems, and astable, which is particular to bound-bound systems at intermediate coupling strength. Contrary to previous expectations, the signatures of the quantum interference structures in pump-probe delay traces were found to be robust toward averaging over initial quantum states. It was shown that the spectral variations observed while tuning the pump pulse wavelength is a quantum matter-wave relative of the fringes observed in a pulsed optical Michelson interferometer.

DOI: 10.1103/PhysRevA.70.033418 PACS number(s): 42.50.Md, 82.20.Gk, 03.75.−b, 82.53.Hn

I. INTRODUCTION

State level crossing is a general quantum mechanical phenomenon appearing in basically all fields of natural science. Prominent examples include neutrino flavor conversion [1], nuclear reactions [2], chemistry in interstellar space [3], and vision and other biological light harvesting processes [4]. Consequently, attaining a thorough understanding of the basic dynamics in such processes has been a long-standing effort in physics including pivotal studies by Landau [5] and Zener [6].

Clearly, the result of a crossing event is dependent on the relative time scales for mixing of the coupled states and traversal of the crossing region. Choosing the coupled states as representation, it is often convenient to define the adiabaticity of the process, $\gamma \equiv V/\nu_+^{ad}$, where V is the coupling between the two diabatic states and ν_+^{ad} the vibrational frequency of the upper adiabatic state. Two limiting cases are then easily discerned. In the adiabatic limit $\gamma \to \infty$, a system starting in one adiabatic state exits the crossing still in the initially populated state. The reverse outcome, the system going to the initially unpopulated adiabatic state, is obtained in the opposite limit $\gamma \to 0$. It is in this case generally more convenient to change representation to the diabatic uncoupled states. In either limit the quantum state representation is clear with well-defined basis sets and small coupling matrix elements between the corresponding states, and the crossing events are well described by perturbative methods. Pure limiting cases in nature are scarce, though, and understanding and accounting for the effects of deviations from them is a key topic, as reflected in, for instance, the considerable interest in nonadiabatic effects in molecules in the chemical physics community [7–12]. The most challenging case then, as always, is in the intermediate $\gamma \approx 1$ range when neither limiting description is adequate and the primary crossing process seems to be best viewed as a strong mixture of the two asymptotic cases [13,14]. In the following, we call this the fully coupled case.

Within the particular framework of molecules, the intermediate coupling situation represents the worst instance of breakdown of the Born-Oppenheimer approximation to decouple the motion of electrons and atomic nuclei. It thus paves the way for strong dynamical, i.e., nonadiabatic effects on the electronic state evolution and, consequently, the molecule's chemical properties. These dynamical effects have been little explored by direct experiments, however. Stolow and co-workers [15,16] performed the first real-time studies of a system in this coupling strength range, the bound-unbound state interaction in predissociation of the IBr ($B\,^3\Pi_{0+}$) state. An investigation of a bound-bound state system, $Rb_2(A\,^1\Sigma_{u0}^+ \sim b\,^3\Pi_{u0})$, was recently published by us [17].

For the bound-unbound system pronounced long-lived resonances with distinct vibrational frequencies are observed at certain excitation wavelengths [15,16]. These resonances were explained qualitatively as arising from interference between wave packets traveling along adiabatic and diabatic trajectories analogous to the mechanism of adiabatic trapping in strong-field photodissociation [18]. Other authors interpreted results from similar systems in terms of interference between either adiabatic [19] or diabatic wave packets [20,21]. The interference nature of these long-lived resonances is clearly demonstrated by the oscillation in wave-

*Electronic address: tony.hansson@physto.se

packet lifetime occurring as either the pump wavelength is tuned [15,16,19–22] or the potential curves are altered [20]. In the former case, essentially, the mean wave-packet momentum is varied, whereas by the latter method the relative path difference is changed and the formal similarity to Stückelberg oscillations in particle scattering probabilities was pointed out [20]. The dependence of these interference "fringes" on coupling strength was investigated in Ref. [23]. In a semiclassical path integral model, finally, the resonances occur for any coupling strength whenever an adiabatic bound level and a diabatic one are degenerate [24] which for IBr was found to be a propensity rule rather than a strict one [22].

The same kind of diabatic-adiabatic hybrid wave-packet trajectory resulting in long-lived resonances in the predissociation case we [17] demonstrated to exist also in the bound-bound system. We concluded, moreover, that the signature of this mesobatic motion, a term introduced by us, was observed in the experimental pump-probe data. The situation is more complicated in the bound-bound system, however. Instead of the single mesobatic trajectory in the bound-unbound case, there are in this system four possible flavors of the same type, depending on which side of the crossing and in which electronic state the trajectory has its single turning point. The four trajectories, moreover, are not independent but come in pairs, the members sharing the forked part of the path, for which the mesobatic conditions necessarily are satisfied simultaneously.

We provide here a deepened and broadened analysis of the bound-bound state intermediate case quantum wave-packet dynamics, as studied in the $Rb_2(A \sim b)$ system. Most importantly, we provide more experimental data and extend the quantum dynamics simulation to facilitate direct comparison with the thermally averaged experimental pump-probe traces. We show that also at the elevated molecular temperatures in the experiments the observed traces are characterized mainly by dynamical interference structures of the mesobatic kind. We further identify two types of mesobatic motion: *bistable*, which corresponds to the one previously reported in both bound-unbound and bound-bound systems, and *astable*, which is particular to bound-bound systems at intermediate coupling strength. The signatures of these dynamical quantum interference structures in pump-probe delay traces are found to be robust toward averaging over initial quantum states, which stands in contrast to expectations for the bound-unbound system [19,20]. Finally, we show that the spectral variations observed while tuning the pump pulse wavelength, as in the bound-unbound system [15,16,19–22], are a quantum analog of the fringes observed in a pulsed optical Michelson interferometer. Here, both the total energy of the wave packet and the rotational state dependence of the potential curve shapes serve to introduce the required change in quantum phase difference along the two paths in the forked part of the mesobatic trajectories.

The rest of this article is laid out as follows. In Sec. II we present the molecular system and the employed theoretical and experimental methods. This is followed in Sec. III by a presentation of the primary experimental and theoretical results. The discussion of these results in Sec. IV is divided into four parts. It starts with an overview and qualitative discussion of the measured and calculated pump-probe traces. Having established the adequacy of the calculations, the trace frequency spectra are decomposed into initital quantum state contributions and shown to consist of mainly variations of two basic spectra, each corresponding to regular beating in the pump-probe signal. The basic spectra, next, are assigned to quantum wave-packet dynamics of the mesobatic kind. Finally, the signatures of the mesobatic motions in the experimentally observed data are identified and the rotational state dependence of the potential curve shape is shown to offer access to a pulsed quantum matter-wave Michelson interferometer. The paper is concluded in Sec. V.

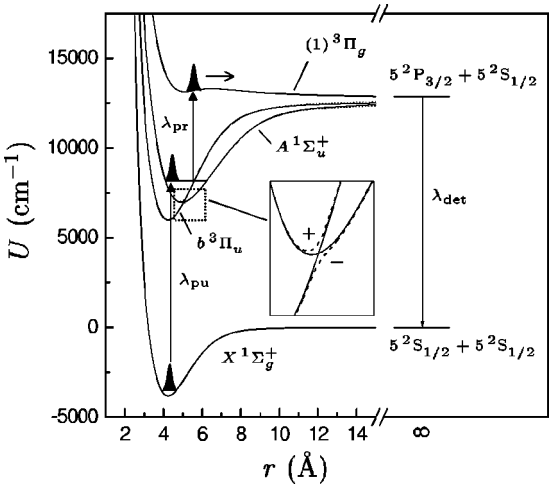

FIG. 1. Potential energy curves of Rb_2 [27] and the pump-probe measurement scheme. The pump wavelength $\lambda_{pu}=865-942$ nm and the probe wavelength $\lambda_{pr}=1700$ nm. Atomic $D2$ line emission at $\lambda_{det}=780$ nm is detected. Inset: magnified view of the level crossing region and labeling of the adiabatic curves (broken lines).

II. METHOD

A. Molecular system and pump-probe scheme

The $Rb_2(A\,^1\Sigma_{u0}^+ \sim b\,^3\Pi_{u0})$ system is shown in Fig. 1. In Hund's case (a) representation the A and b states cross at an internuclear separation of $r^{\times}=5.1$ Å and both go to the $5s+5p$ separated-atom limit. As in the other homonuclear diatomic alkali-metal molecules, these states couple by spin-orbit (SO) interaction [25] with respect to which they here are assumed diabatic. For the A state $\Omega=0$ and, due to the $\Delta\Omega=0$ selection rule for the interaction, only this component of the b state is directly involved. The various Ω components of the b state couple to each other through the spin-uncoupling operator [26]. This strength, however, we estimate to be several orders of magnitude smaller than the spin-orbit splitting of the components and, therefore, the $\Omega=1$, 2 components may be disregarded. Diagonalizing the SO interaction matrix for this reduced system, one obtains two Hund's case (c) relativistic adiabatic states of 0_u^+ symmetry correlating to the $5\,^2P_{1/2,3/2}+5\,^2S_{1/2}$ atomic limits. Being the lowest excited ungerade states, A and b are not expected to be significantly perturbed by any other states.

The SO coupling matrix element $V_{Ab}(r)$ was calculated *ab*

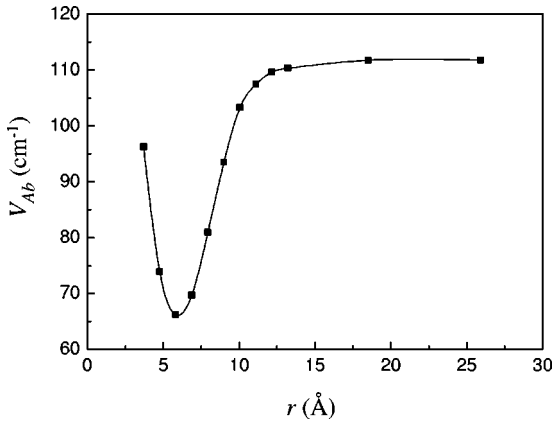

FIG. 2. Spin-orbit coupling strength V_{Ab} as a function of internuclear separation r obtained in Ref. [31] by scaling the corresponding curve for Cs_2. The solid curve is a spline fit to the points.

initio by Edvardsson *et al.* [25]. Its dependence on the internuclar separation r is substantial and in accordance with other diatomic homonuclear alkali-metal molecules [28–30]. The calculated magnitude of the coupling seems unreliable, though, as the values for the separated atoms are already about 30% too low. In fact, this is about the same factor needed to bring the molecular *ab initio* SO coupling in accordance with the estimate [31], based on scaling of the Cs_2 coupling element, shown in Fig. 2. This estimate agrees with high-resolution spectroscopic data pertaining to internuclear distances well beyond the crossing region [32] and, in the absence of other guidance as to which is the best representation of the actual situation in the crossing region, we have chosen here to use the estimated curve. The estimated value 70 cm^{-1} of the SO coupling at the curve crossing $V_{Ab}^{\times}$ corresponds to $\gamma_{Ab}=1.5$. This is in the intermediate coupling strength range, which is in accordance with conclusions from studies of calculated rovibrational wave functions [31]. Consequently, neither the adiabatic nor diabatic picture of this system is adequate and we arbitrarily choose in the following to use mostly the Hund's case (a) $\{A,b\}$ labeling of the states. Whenever we refer to the relativistic adiabatic representation $\{+,-\}$ denote the upper and lower 0_u^+ states, respectively.

To bring out the quantum wave-packet dynamics in this fully coupled bound-bound state system we applied the pump-probe scheme sketched in Fig. 1. A pump pulse launches a wave packet at the inner turning point of the A state, the kinetic energy of which may be varied within about 500 cm^{-1} by tuning the pump pulse wavelength. This wave packet then moves toward the crossing region where it may undergo intersystem crossing to the b state. After some time delay τ the probe pulse interrogates the wave function at the outer turning point of the b state by projecting part of it onto the unbound $(1)^3\Pi_g$ state, the latter state correlating adiabatically to the $5\,^2P_{3/2}+5\,^2S_{1/2}$ limit. Monitoring the intensity of the atomic $5\,^2P_{3/2}\rightarrow 5\,^2S_{1/2}$ ($D2$) line emission as a function of τ we thus obtained real-time traces of the quantum dynamics as viewed through a detection window in the b state. No atomic $D1$ fluorescence was detected, in accordance with the assumed detection mechanism.

We are in the present context concerned with only radial wave-packet dynamics and the experiments were performed

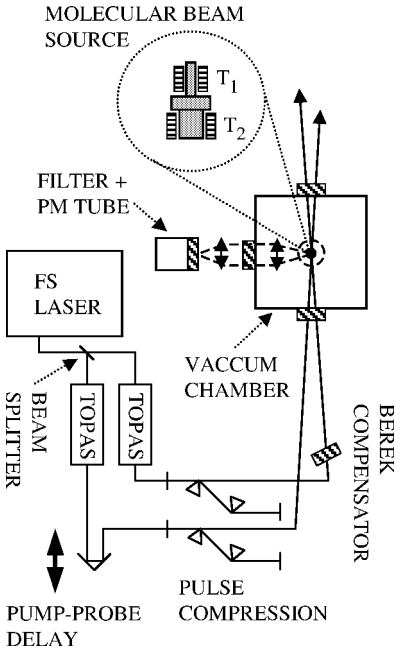

FIG. 3. Schematic experimental setup. Note that the molecular beam propagation is directed perpendicularly out of the plane of the figure. FS LASER is the femtosecond pump laser. T_1 (exit) and T_2 (sample container) indicate the two separately heated chambers of the molecular beam source. PM TUBE is the photomultiplier tube.

at the nominal magic angle of 55° between pump and probe polarizations. As emitted light was collected in a definite direction, although over a substantial solid angle, this requires the detected fluorescence to be emitted isotropically, which is, generally, not true for the pump-probe detection scheme applied here. The depolarization of the $D2$ fluorescence due to hyperfine interaction in the rubidium atom, however, is sufficiently strong to ensure approximately isotropic detection conditions [33].

B. Experiment

The experimental configuration, shown schematically in Fig. 3, comprised a standard femtosecond pump-probe spectroscopy setup coupled to a molecular beam apparatus with fluorescence detection.

The Rb_2 beam was generated in a vacuum chamber, background pressure under operation $<5\times10^{-6}$ mbar, by a two-chamber oven containing solid rubidium metal (>99.9% purity, natural isotope composition, Chemetall). The temperature of each chamber was separately adjustable allowing individual control of total Rb vapor pressure and Rb_2 content, respectively. At operation temperatures around 700 K a mild cooling of the beam occurs as it expands through the $\varnothing 50$ μm nozzle, somewhat affecting the rotational temperature of the molecules, T_{rot}. The limited pump pulse bandwidth, however, is the dominating factor restricting the effective T_{rot} of the excited population to about 400 K [33]. We expect no significant cooling of the vibrational degree of freedom to have taken place.

The pump and probe light beams intersected each other at an angle of about 2° and the molecular beam perpendicularly

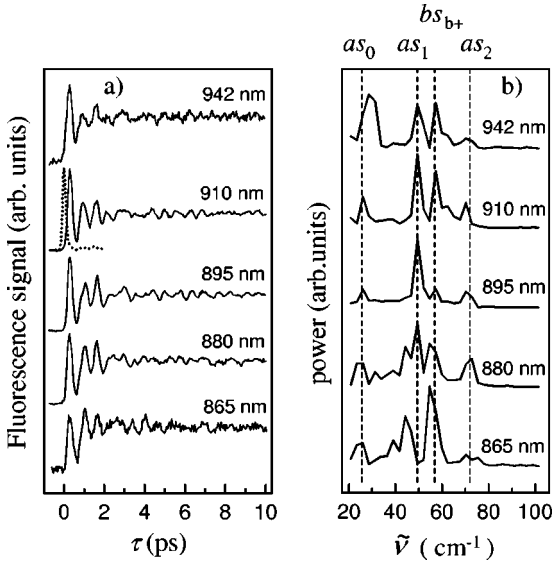

FIG. 4. (a) Measured pump-probe delay traces, for indicated λ_{pu}, normalized to similar peak intensity. For all traces λ_{pr} = 1700 nm. Dotted line: cross-correlation trace of the pump and probe pulses. (b) Corresponding power spectra individually rescaled to facilitate comparison. Vertical broken lines mark frequencies characteristic of bistable (bs_{b+}) and astable (as_0, as_1, as_2) mesobatic wave-packet trajectories.

at a point 4 mm downstream of the oven nozzle. Fluorescence emanating from this point in a direction perpendicular to the two light beams as well as the molecular beam was collected and collimated by an $f=+50$ mm lens. The collimated fluorescence light was transported through a window to the air side and imaged, with overall $f_{\#} \approx 1.3$, through a narrowband interference filter (780 or 795 nm, $\Delta\lambda_{FWHM}$ = 10 nm) onto a red-sensitive photomultiplier tube (Hamamatsu, R928). Of the atomic rubidium $D1$ and $D2$ lines only the latter was detectable. A gated photon counter (Stanford Research, SR400) registered pulses incurring for 1000 laser pulses for each pump-probe delay setting.

The pump and probe light pulses were synchronously generated, each by an optical parametric amplifier (Light Conversion, TOPAS IV) pumped by approximately half the output from a femtosecond pump laser (Clark-MXR, CPA2001). The probe pulse, held fixed at 1700 nm, was obtained as the idler pulse from one of the TOPAS's, while the pump pulse at 865–942 nm was produced by frequency doubling of the idler from the other TOPAS. The spectral bandwidth of each pulse was about 120 cm^{-1}. The zero pump-probe delay was established and temporal cross correlation between the pump and probe pulses were measured *in situ* by $2\times\lambda_{pu}+1\times\lambda_{pr}$ nonresonant excitation of atomic $7\,^2P \rightarrow 5\,^2S$ fluorescence. The cross correlation was found to be characterized by a full width at half maximum of 190 fs; see Fig. 4. It is slightly asymmetric, however, due to some molecular process giving a small oscillating signal at positive delays, indicating that the true cross correlation width was somewhat smaller. Each light beam was weakly focused by an $f=+500$ mm lens and its intensity minimized in order to avoid saturation and nonresonant multiphoton effects while keeping sufficient pump-probe signal level. The relative linear polarization orientation between the two beams was adjusted to 55° by means of a Berek compensator (New Focus, 5540). Polarization purities were better than 100:1. The pump and probe pulse delay, finally, was adjustable in 3.3 fs steps through a retroreflector mounted on a stepping motor controlled translation table. We used in the present study a step length corresponding to 50 fs delay change.

The experimental traces presented below were obtained by averaging over 20 pump-probe delay scans.

C. Theory

The pump-probe transients were simulated using the fast Fourier transform split-operator method [34–36], which is of second order accuracy in time. An, in principle, arbitrary number of coupled states are allowed for by partitioning the Hamiltonian into sets of pair-wise coupled states. Four states were used in our simulations: $X\,^1\Sigma_g^+$, $A\,^1\Sigma_u^+$, $b\,^3\Pi_u$, and $(1)\,^3\Pi_g$. The Hamiltonian was discretized on a spatial grid with 512 grid points ranging from 2.6 to 12 Å. All radiative transition moments were assumed to be of electric dipole type and r independent.

The pump-pulse-molecule interaction was modeled by explicit time propagation of an initial rovibrational level $|v_0 J_0\rangle$ in the X state coupled by the radiation field to the A state. This is in Hund's case (a) the only allowed one-photon process involving the electronic ground state. A time step of 0.5 fs was used during the on time of the pump pulse, which was increased to 5 fs in the subsequent field-free wave-packet propagation in the $A\sim b$ system. The probe pulse was assumed to couple only the b and $(1)\,^3\Pi_g$ states and the pump-probe signal was obtained by application of the Rosen-Zener (RZ) approximation [37,38]. Thus, the signal at a time delay τ was calculated from the instantaneous population within a probe window in the b state determined by the transition difference potential and probe pulse wavelength and duration. The RZ model is accurate when the laser pulse duration is short compared to the time scale of wave-packet dynamics.

The experiments were performed with the linearly polarized pump and probe pulses set at magic angle configuration. This ensures that the molecular rotation influences the wave-packet dynamics only through an additional centrifugal term to the potential energy curves, $\hbar^2 J(J+1)/(2\mu r^2)$, for the reduced molecular mass μ. The molecular temperature in the experiments was high, furthermore. Thus, on the average, any optically induced change in J is small compared to J itself, which allowed for reducing the calculational time by setting $\Delta J=0$ for all optical transitions. The total pump-probe transient, finally, was obtained by incoherent summation over the thermally weighted initial state distribution.

In the simulation results presented here, a set of initial states $\{|v_0=0-15, J_0=0-300\rangle\}$ at a temperature of 700 K was used and the light pulse intensity profiles were Gaussian with 120 fs full width at half maximum (FWHM). Two different sets of potential curves taken from Refs. [25,27] were used. For both sets the $b\,^3\Pi_u$ curve was down-shifted by 80 cm^{-1} taking into account diagonal spin-orbit coupling in the free-precession approximation [26]. For the set of curves

by Edvardsson *et al.* [25] the $(1)^3\Pi_g$ was missing and was taken from Ref. [27]. Finally, all calculations were done with $V_{Ab}(r)$ as displayed in Fig. 2.

III. RESULTS

Our primary results comprise two parts, measured pump-probe delay traces and their quantum dynamical simulation for a thermal ensemble of molecules.

Measured traces at various pump wavelengths but fixed probe wavelength can be seen in Fig. 4(a). Overall, from negative to positive delays, the traces first display a sharp rise of the signal from zero level to a peak at about 280 fs delay. This is followed by a short-lived large-amplitude oscillatory feature and leveling out at half or more of the first peak's intensity with superposed smaller-amplitude oscillations, the latter extending well beyond the displayed 10 ps (see Ref. [17]). The molecular origin of these traces was ascertained by increasing the nozzle temperature in which case the corresponding signal vanished, as required by the corresponding shift of thermal equilibrium of the Rb gas towards lower molecular concentration.

The power spectra of the traces, Fig. 4(b), show that for $\lambda_{pu}=942-880$ nm there are four characteristic frequencies at 25, 49, 56, and 72 cm^{-1}, respectively, whereas the trace for $\lambda_{pu}=865$ nm yields slightly lower values of the middle peaks, 45 and 54 cm^{-1}. As motivated and explained below, we have assigned these peaks to either bistable mesobatic wave-packet motion in the diabatic b and adiabatic "+" states, bs_{b+}, or astable motion at the ground frequency ν_{as_0} with its first and second overtones, as_1 and as_2, respectively. These four peaks correspond to $b+$, α, β, and γ in Ref. [17]. Of particular interest to the following discussion is the change in spectral peak intensities as λ_{pu} changes from 942 to 865 nm, the outstanding feature being the strong modulation of the bs_{b+} peak. Note, these spectra, like all others in this article, have been obtained as the absolute square of the fast Fourier transform of the trace range 1.5 to 10 ps.

Results of calculations using the set of potential curves by Park *et al.* [27] are shown in Fig. 5. The conditions for the simulations were chosen such as to be comparable to those of the experiments and we note that, qualitatively, all characteristic features of the experimental traces are well reproduced. The comparison is particularly favorable for $\lambda_{pu}=910$ nm (see Fig. 6), in which case calculated and measured traces agrees well also on a quantitative level, and this pump wavelength is used below as a "showcase" in the analysis of the quantum wave-packet dynamics. It is the most favorable instance, however, and, generally, the agreement between experiment and theory is less good. Accordingly, shifting attention to the frequency domain, the power spectra in Fig. 5(b) present differences in detail between theory and experiment. The experimentally observed peaks are reproduced at the correct positions, including the downshift in frequency of the as_1 and bs_{b+} peaks at $\lambda_{pu}=865$ nm. Except in the $\lambda_{pu}=910$ nm showcase, however, the relative peak intensities are not very similar to the experimental ones, when compared at specific pump wavelengths. The experimentally observed general modulation of the bs_{b+} peak, nonetheless, is reproduced but the minimum for $\lambda_{pu}=895$ nm in the experiments has been shifted to 942 nm in the calculations. As another point of difference, we note that in the calculations also the as_1 peak is modulated, which contrasts with its rather constant amplitude in the experimental spectra.

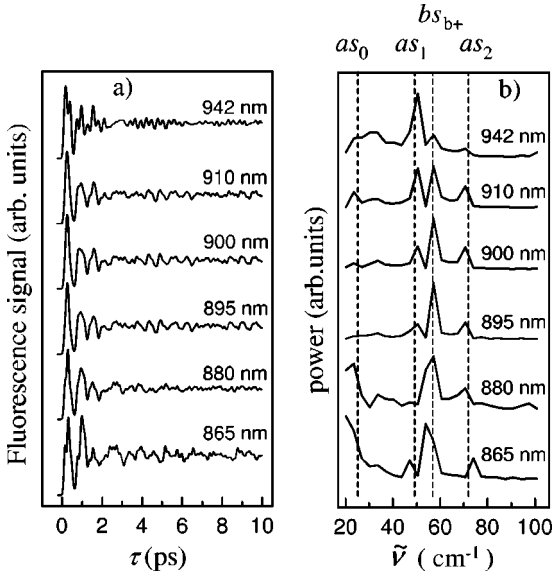

FIG. 5. (a) Calculated pump-probe delay traces, for indicated λ_{pu}, using the potential energy curves from Ref. [27]. (b) Corresponding power spectra individually scaled to facilitate comparison. Vertical broken lines mark frequencies characteristic of bistable (bs_{b+}) and astable (as_0, as_1, as_2) mesobatic wave-packet trajectories.

The sensitivity of the theoretical results to the choice of potential energy curves can be appreciated by comparing Figs. 5 and 7. The results were obtained with identical parameter choices and V_{Ab}(r) but different sets of potential energy curves by, respectively, Park *et al.* [27] and Edvardsson *et al.* [25]. Qualitatively, the results in Fig. 7 compare well with both the other calculation and the experiments. Note, however, that the relative intensities of the spectral peaks differ significantly among all cases.

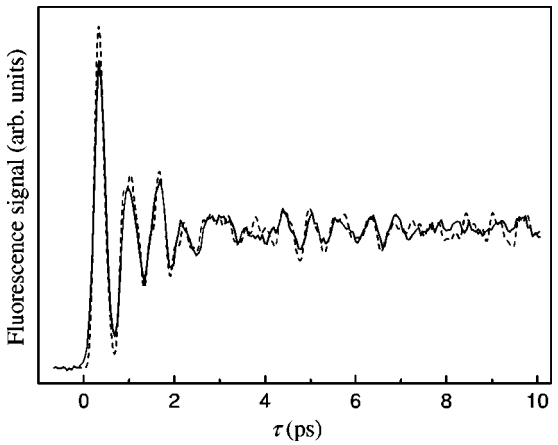

FIG. 6. Measured (solid) and calculated (broken) pump-probe delay traces from Figs. 4(a) and 5(a), respectively, for $\lambda_{pu}=910$ nm.

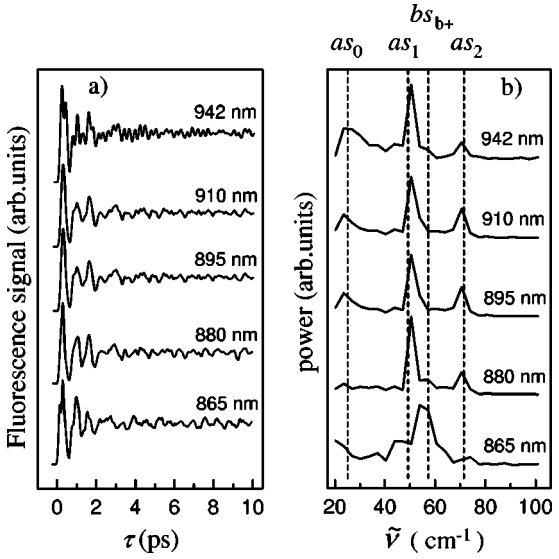

FIG. 7. (a) Calculated pump-probe delay traces for indicated λ_{pu} using potential energy curves from Ref. [25]. (b) Corresponding power spectra individually scaled to facilitate comparison. Vertical broken lines mark frequencies characteristic of bistable (bs_{b+}) and astable (as_0, as_1, as_2) mesobatic wave-packet trajectories.

Calculations were done to probe also the dependence of the calculated data on the choice of spin-orbit coupling model and strength. We thereby established that the dependence of the spin-orbit coupling element V_{Ab} on internuclear separation was nonconsequential for the thermally averaged data, the difference in signal between an r-dependent and a constant V_{Ab} being less than 1.5% over the whole delay range for $\lambda_{pu}=910$ nm. The magnitude of the spin-orbit coupling at the potential energy curve crossing, on the other hand, was highly influential. A change from 70 to 75 cm^{-1} was sufficient to alter the 910 nm spectrum in Fig. 5(b) to something similar to the 895 nm spectrum in the same figure, consisting in mainly the bs_{b+} peak.

IV. DISCUSSION

Our aim in this section is to extract and interpret the quantum wave-packet dynamics underlying the presented pump-probe traces. A characteristic and regular rotational state dependence of the calculated pump-probe spectra was found and shown to originate in interference between quantum wave packets moving synchronously along a diabatic and an adiabatic path. Two general kinds of such motion were identified. These were analyzed within a semiclassical model and shown to make the dominating contributions to the pump-probe traces. The overall system may be seen as a quantum matter-wave relative of a pulsed optical Michelson interferometer.

A. Thermally averaged traces and spectra

As starting point in the analysis of the results we take verification of the experimental pump-probe scheme and assessment of the accuracy of the simulations.

Turning first to the verification of the assumed pump-probe trace, we note that the most characteristic features of the experimental pump-probe delay traces in Fig. 4(a), the initial delay of the the signal onset and the pump wavelength dependence of the initial wave-packet splitting ratio, are reassuringly consistent with the scheme sketched in Fig. 1.

Take the initial signal delay. Launching a wave packet on the inner side of the A potential curve and probing it close to the outer turning point in the b state, we would expect a delay of the signal onset equivalent to half a vibrational period in the upper adiabatic curve. The thus estimated delay of 290 fs matches well within experimental uncertainty the observed 280 fs.

The increase of wave-packet energy as λ_{pu} is decreased, next, would be expected to affect the appearance of the traces in three ways, all of which are observed in Fig. 4, except for the $\lambda_{pu}=942$ nm trace which seems to be a special case. First, the intensity of the first peak is dependent on the fraction of the total wave packet proceeding to the probe point. This fraction, in turn, depends on the degree of adiabaticity of the curve crossing which decreases with kinetic energy, leading to a reduced peak height. The wave-packet trajectory, second, is extended to outer turning points at larger r, while the probe window position is held fixed by λ_{pr}. Thus, a broadening of the first peak would be expected as the turning point is gradually moved out of the probe window. Third, the anharmonicity of the potential curves would lead to the increased wave-packet vibration period seen in Fig. 4(b).

The trace for $\lambda_{pu}=942$ nm does not quite follow this pattern. There is also an unusually large peak around 30 cm^{-1} in its power spectrum. These deviations we attribute to the fact that the launched wave packet is close to the bottom of the A state and at an energy level close to the curve crossing, which invalidates our, in essence, semiclassical arguments.

The rapid leveling out of the pump-probe delay trace, finally, is consistent with the strong spin-orbit mixing of the A and b states at the crossing, the interaction strength presumably being in the intermediate range.

A critical component in the calculations is the spin-orbit coupling V_{Ab}. The calculations employed an r-dependent V_{Ab} but, as stated in the Results section, the variation with r was found inconsequential for the thermally averaged signal. The magnitude of the coupling, on the other hand, was found to be of great importance. We show below that the immunity of the signals to the V_{Ab} r dependence is not general but derives from the special character of the wave-packet trajectories making the biggest contributions to the thermal signals. The signal dependence on the coupling magnitude, obviously, is a general feature.

All in all, the measured traces comply qualitatively with the pump-probe scheme presented in Sec. II A. This assignment is reinforced by the good quantitative agreement between the theoretical and experimental data for the 910 nm showcase in Fig. 6. The agreement is less favorable for other pump wavelengths. Note, however, that the deviations do not relate to the qualitative features of the delay traces or spectra. What does differ, essentially, is the relative amplitudes of the spectral components in the signal, which, we will see below, depend critically on a quantum phase difference arising in

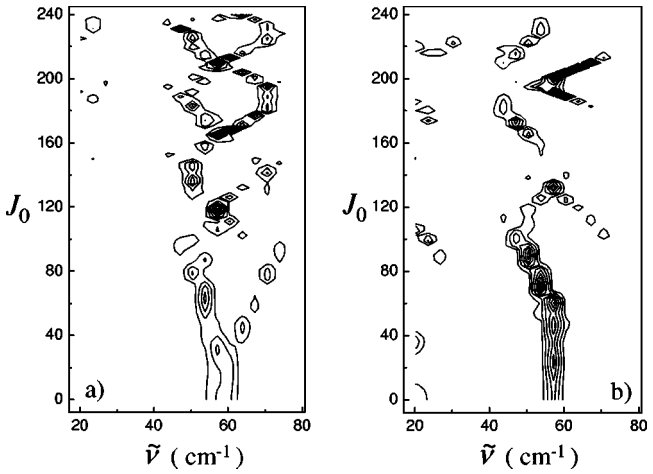

FIG. 8. Power spectra of calculated pump-probe delay traces, with thermal population and pump transition weighting of initial states removed, as a function of J_0 for $\lambda_{pu}=910$ nm. (a) $v_0=0$; (b) $v_0=6$.

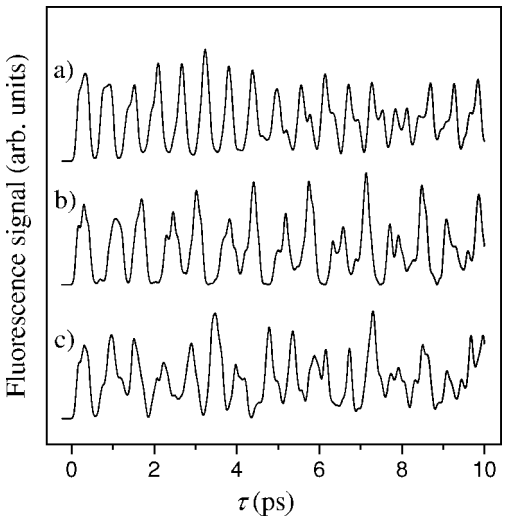

FIG. 9. Calculated pump-probe delay traces for $\lambda_{pu}=910$ nm and $v_0=6$. (a) $J_0=57$; (b) $J_0=96$; (c) $J_0=81$.

propagation along different wave-packet paths. This is, with the present accuracy of potential energy curves and couplings, a too fragile parameter to make a detailed multiparameter fit of the experimental data meaningful. Thus, we aim here at a qualitative understanding and interpretation of general quantum wave-packet dynamics rather than at obtaining accurate data on the Rb_2 molecule.

B. Composition of thermal spectra

The simulation result in Fig. 6 exhibits good agreement with the measured pump-probe trace. Thus, we take the calculated quantum wave-packet dynamics in this case to represent well what is going on in the physical system and, to gain further insight into the processes, we decompose the calculated pump-probe power spectrum into initial state contributions. The averaged spectrum is found to result mainly from two characteristic types, each corresponding to regular wave-packet motion, to be analyzed in Sec. IV C.

Figure 8 displays the rotational state dependence of the calculated pump-probe spectra for two choices of initial vibrational state. To bring out more clearly the characteristic variations of the spectra with initial state, the weighting of the spectra according to thermal population and optical transition probabilities has been removed. The outstanding feature in both cases is the quasiperiodic spectral appearance with J_0, most obvious when looking for the presence of the bs_{b+} peak, which appears alone and repeatedly splits and recurs with changing J_0. Note the difference in "phase" of the quasioscillation in the two cases, most conveniently seen as the difference in J_0 for which the bs_{b+} peak appears. Finally, we note that the as_{0-2} peaks anticorrelate with the bs_{b+} peak as they always appear in between two occurrences of the bs_{b+} dominated spectrum. All these features are typical and appear similarly for other pertinent choices of v_0 and λ_{pu}.

There is, thus, a characteristic variation in the signal spectrum with rotational quantum number which would be expected to correspond to a likewise characteristic variation in wave-packet dynamics. This, indeed, is the case and we show in Fig. 9 three representative traces. Figure 9(a) shows a situation when bs_{b+} is dominating the spectrum. As expected, a rather regular beating at the bs_{b+} frequency is observed. In Fig. 9(b) the signal from the opposite case, that is, when the spectrum is dominated by the as_{0-2} triplet, is shown. Again, the trace is dominated by a single beating, now with a period corresponding to, basically, the as_0 frequency, but the peaks are strongly split by 640 fs and modulated by the as_1 and as_2 beats. The intermediate case in Fig. 9(c), finally, does not display any clear regularities. We wish here to focus on the composition of the pump-probe spectra and leave the discussion of the quantum wave-packet dynamics behind these typical traces to Sec. IV C.

Having established the character of the pump-probe traces and spectra for individual initial states, to see how they contribute to the total pump-probe spectra we need to reintroduce the weighting according to initial thermal population and pump transition probability. As seen in Fig. 10, which should be compared to Fig. 8, the most obvious effect of the weighting is to enhance the importance of a range of rotational states. The position of the window in J_0 is determined by λ_{pu} so varying pump wavelength amounts to scanning over regions of different types of spectra or, equivalently, wave-packet dynamics.

To understand how the individual initial-state related pump-probe spectra contribute to the total one, it should be realized that the power spectra in Fig. 10 do not contain information on the relative phase of the frequency components. This phase, however, will be consequential in summing contributions from a range of initial quantum states and must be considered. As it turns out, the phases of most spectral components, except those belonging to bs_{b+} and as_{0-2}, vary strongly with J_0 and average to zero. The power spectra after summing over rotational states (see Fig. 11), therefore, consist almost exclusively of the bs_{b+} and as_{0-2} peaks. Due to the presence of the pump pulse window in J_0, the relative intensities of the peaks vary with v_0 and the total pump-

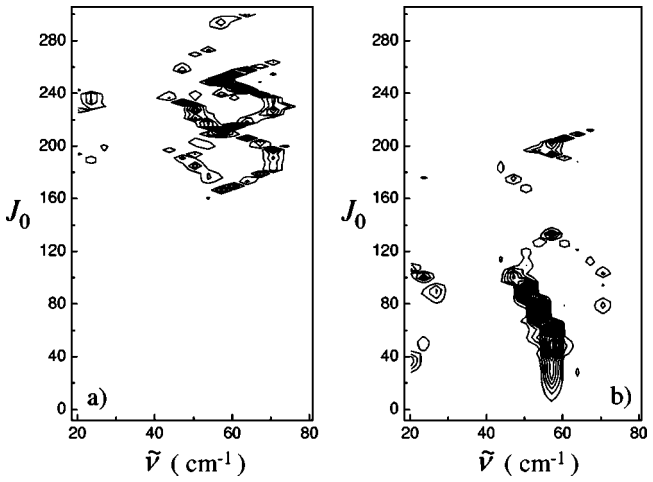

FIG. 10. Power spectra of calculated pump-probe delay traces weighted according to thermal population and transition probability, for λ_{pu}=910 nm, as a function of J_0. (a) v_0=0; (b) v_0=6.

probe spectra comprise superpositions of varieties of the two basic ones. It follows that we can interpret the observed λ_{pu} dependence of the experimental spectra in Fig. 4(b) as being due to sliding of the excitation window across J_0 regions with different compositions of the archetypal kinds of spectra or, equivalently, quantum wave-packet motion.

A final note on the composition of the total pump-probe spectrum concerns the dependence of the spin-orbit coupling strength on internuclear separation. As noted in the Results section, this dependence had in the calculations very little effect on the thermally averaged data. This was, however, not wholly so for the data as decomposed into initial states; namely, the traces like those exemplified in Figs. 9(a) and 9(b) were largely insensitive to such a variation with r, whereas the intermediate case [Fig. 9(c)] did exhibit a substantial sensitivity to it. Quite naturally, all three kinds of traces depended strongly on the magnitude of the coupling at the crossing point. The bs_{b+} and as_{0-2} dominated spectra, thus,enjoyed a certain robustness toward the r dependence of V_{Ab}. This taken together with the fact that these two kinds of

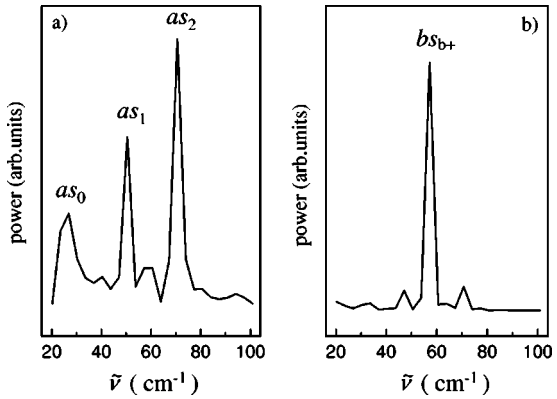

FIG. 11. Power spectra after summation over J_0 of calculated pump-probe delay traces weighted according to thermal population and optical transition probability for λ_{pu}=910 nm. (a) v_0=0. (b) v_0=6.

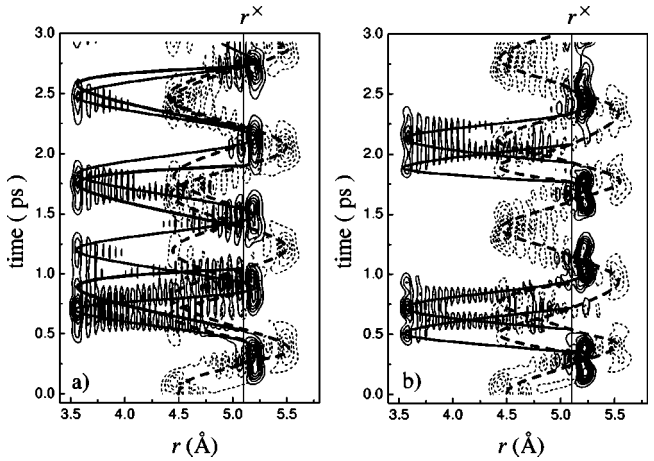

FIG. 12. Wave-packet evolution corresponding to the two basic signal traces in Figs. 9(a) and 9(b), respectively. Shown is the absolute square of the wave function in the diabatic representation and broken and solid contours relate to A and b state projections, respectively. Thicker lines indicate approximate classical trajectories for the two wave-packet fractions going into the A (broken) and b (solid) states in the first passage of the curve crossing. (a) bs_{b+} case, J_0=57: bistable mesobatic motion. (b) as_{0-2} case, J_0=96: astable mesobatic motion.

spectra dominated the total spectra accounts for the insensitivity also of the latter toward the variation of the spin-orbit coupling strength with internuclear distance.

C. Quantum wave-packet dynamics

The pump-probe signal, we have seen, comprises a thermal average in which only two characteristic spectra appear to a significant degree. One of the spectra consists in mainly the bs_{b+} peak and corresponds to a signal, in the time domain, like that in Fig. 9(a). The other spectrum is the as_{0-2} triplet yielding the split beating of as_0 period in Fig. 9(b). Note the regularity of this triplet indicating that $\tilde{\nu}_{as_0}$ is the fundamental frequency and that $\tilde{\nu}_{as_1}$ and $\tilde{\nu}_{as_2}$, respectively, are the first and second overtones of it. In this section we give an interpretation of these basic spectra in terms of two distinct subclasses of hybrid diabatic-adiabatic or, more briefly, mesobatic [17] quantum wave-packet dynamics.

The wave-packet dynamics underlying the two archetypal traces [Figs. 9(a) and 9(b)] are shown in Fig. 12. From Fig. 12(a), it can be seen that the regular beating at the bs_{b+} period arises in a situation of evolution of two essentially decoupled wave-packet trajectories along the sketched classical paths; namely, at the first encounter of the crossing region the wave packet splits in two parts, one that proceeds to the outer turning point of the b state while the other goes to the A state outer turning point. Returning to the crossing, the two fractions have been separated in time and the total wave-packet evolution, at least for a while, can be decomposed into the respective evolutions. Picking the detected b part of the wave packet, we see that, classically, the wave-packet fractions generated at the inbound crossing would return next time simultaneously to the crossing region. This facilitates quantum interference and in this particular case the

initial b fraction at the outer turning point is recreated with negligible part being transferred to the A state. The nascent A wave-packet fraction can be seen to be restricted to a similar type of trajectory with its only outer turning point in the A state.

Hence, although, as evidenced by the very first curve crossing event, the transition probability into the two channels without interfering wave-packet fractions is almost equal, we have in Fig. 12(a) a situation where quantum interference at subsequent crossing encounters effectively closes one of the channels. By this, the b wave-packet fraction is trapped in a coherent concerted motion along the diabatic b and adiabatic "+" paths yielding a signal beating at a frequency of $\tilde{\nu}_{b+}=\tilde{\nu}_{+}=\tilde{\nu}_{b}$. This is the mesobatic motion we [17] previously identified and denoted S_{b+}. The corresponding A wave packet, similarly, moves in its S_{A-} trajectory along the diabatic A and adiabatic "−" paths.

To gain further insight into and understanding of the mechanism behind the channel closure, we employed a semiclassical framework similar to applications in the bound-unbound case [19,20]. Momentarily ignoring the A fraction, we can picture the inbound b wave packet encountering the crossing where it splits into two parts. The fractions, furthermore, after propagating in different electronic states reappear simultaneously at the crossing and interfere. Then the overall wave function in the adiabatic representation after the second crossing may be written [13]

$$\begin{pmatrix}\psi_{+}\\ \psi_{-}\end{pmatrix}=T_{\times}^{\mathrm{out}}PT_{\times}^{\mathrm{in}}\begin{pmatrix}\psi_{+}^{0}\\ \psi_{-}^{0}\end{pmatrix}, \tag{1}$$

where $T_{\times}^{in}$, P, and $T_{\times}^{out}$ are the matrices describing the wave-function transformation due to the curve crossing in the inward direction, the propagation including turnaround at the inner turning points, and the outward crossing, respectively. Hence,

$$T_{\times}^{\mathrm{in}}=\begin{pmatrix}\sqrt{1-f}e^{i\chi} & \sqrt{f}\\ -\sqrt{f} & \sqrt{1-f}e^{-i\chi}\end{pmatrix}, \tag{2}$$

$$T_{\times}^{\mathrm{out}}=\begin{pmatrix}\sqrt{1-f}e^{i\chi} & -\sqrt{f}\\ \sqrt{f} & \sqrt{1-f}e^{-i\chi}\end{pmatrix}, \tag{3}$$

where f is the nonadiabatic transfer probability and χ the related quantum phase shift. With the phase shift α_j due to propagation along an adiabatic component $j\in\{+,-\}$,

$$P=\begin{pmatrix}e^{2i(\alpha_{+}-\pi/4)} & 0\\ 0 & e^{2i(\alpha_{-}-\pi/4)}\end{pmatrix}. \tag{4}$$

Picking the b wave function, in particular, we set $\psi_{+}^{0}=\varphi(r)e^{-ipr}$, where $\varphi(r)$ is an approximately Gaussian function and p is the mean momentum of the wave packet. Ignoring the A part corresponds to $\psi_{-}^{0}=0$. With these initial conditions,

$$\begin{pmatrix}\psi_{+}\\ \psi_{-}\end{pmatrix}=\begin{pmatrix}(1-f)c_1+fc_2\\ \sqrt{f(1-f)}d\end{pmatrix}\psi_{+}^{0}, \tag{5}$$

where $c_1=e^{2i(\chi+\alpha_{+}-\pi/4)}$, $c_2=e^{2i(\alpha_{-}-\pi/4)}$, and $d=e^{i(\chi+2\alpha_{+}-\pi/2)}-e^{i(-\chi+2\alpha_{-}-\pi/2)}$. Now, it is readily seen that if $d=0$, which occurs irrespective of the f value for $\delta=\alpha_{+}-\alpha_{-}+\chi=n\pi$ for integer n, then the "−" channel is closed for the outbound wave function and all of it goes back to the initial state multiplied by a complex phase factor. Thus, we see that the mesobatic S_{b+} trajectory arises when the overall difference in quantum phase shift along the diabatic b and adiabatic "+" paths is an integer multiple of π.

Similarly, we obtain for the coevolving initial A wave-packet fraction the expression

$$\begin{pmatrix}\psi_{+}\\ \psi_{-}\end{pmatrix}=\begin{pmatrix}\sqrt{f(1-f)}d\\ -(1-f)c_1'+fc_2'\end{pmatrix}\psi_{-}^{0} \tag{6}$$

in which $c_1'=e^{2i(-\chi+\alpha_{-}-\pi/4)}$, $c_2'=e^{2i(\alpha_{+}-\pi/4)}$, and ψ_{-}^{0} is defined similarly to ψ_{+}^{0} above. It is clear that concomitant with the closure of the "−" channel for the b wave packet we should expect an equivalent closure of the "+" channel for the A fraction. A S_{b+} trajectory, hence, is always accompanied by its complement S_{A-}, in accordance with the wave-packet evolution seen in Fig. 12(a).

The wave-packet evolution in Fig. 12(a), thus, is an instance of the case when $\delta=n\pi$. Consequently, at the very first traversal of the curve crossing the wave packet splits into two fractions which, by quantum interference leading to channel closure, are decoupled from each other and from that moment evolve independently for some time restricted by the spreading of the wave packet. Were one under such conditions to probe the wave function at any outer turning point a signal with a frequency identical to that of the corresponding adiabatic state would be obtained. Note, however, it is the *whole* wave packet that is probed. This wave packet is in a well-defined, entangled state of motion consisting of an "adiabatic" wave packet synchronized to a "diabatic" one and can in the intermediate coupling range, obviously, not be classified according to the diabatic/adiabatic scheme. Instead, we have introduced the term mesobatic motion [17]. We wish here to qualify this term and for the particular $\delta=n\pi$ case call it a *bistable* mesobatic trajectory, in analogy to an electronic flip-flop switch being operated in bistable mode. In this mode the switch output can be set to either of two values and then, in the absence of further perturbations, remains indefinitely in that state.

By necessity, we have seen, the S_{b+} and S_{A-} bistable mesobatic trajectories come as a pair. Similar conditions exist under which the complementary S_{b-}/S_{A+} pair may form. These conditions are not met in the studied energy range of the present system, however.

A look at Eq. (5) indicates that provided $f=1/2$, that is, in a perfect intermediate coupling case, there exists a condition $\delta=(n+1/2)\pi$ for which the "+" channel closes for the b wave packet. At the same time, it is readily found, the "−" channel is closed for the returning A fraction. Thus, the evolution of an initial b wave packet would be in the second crossing passage to go wholly into the "−" channel and thus

be transformed into an A wave packet. Now, at the fourth passage of the crossing the wave packet again switches channel and goes into the "+" channel to regain the b character. The reverse process would occur to an initial A wave packet. This kind of motion is in the forked part identical to the corresponding bistable mesobatic trajectory, except that the accumulated quantum phase shift δ is a half integer of π. This forces the wave packet to alternate between outer turning points in the b and A states. We henceforth call this kind of motion an *astable* mesobatic trajectory, once again in analogy with an electronic switch, which in the astable mode oscillates between two output states.

Astable mesobatic wave-packet motion can be seen in Fig. 12(b), which corresponds to the as_{0-2} basic type trace in Fig. 9(b). Again starting the analysis after the very first curve-crossing event we see that, contrary to the bistable case, each of the wave-packet fractions goes to the alternate channel after the first round trip to the inner turning points. As they make the next round trip the initial time shift between the nascent b and A wave packets has been exactly removed, however, and they appear in their inward motion simultaneously and in phase at the crossing. Hence, they must recombine and go back to, except for an overall phase shift, a copy of the very first wave packet launched by the pump pulse at the inner turning point of the A state. At this point the process starts all over. The overall effect in our measured time trace is to produce two beats, each of a fundamental frequency $\tilde{\nu}_{as_0}=(1/\tilde{\nu}_{b+}+1/\tilde{\nu}_{A-})^{-1}$, shifted in accordance with the time difference associated with the round trips from the crossing to the b and A outer turning points, respectively. The phase shift between the beats modulates the spectrum which accounts for the somewhat unusual intensity distribution in Fig. 11 between the fundamental frequency and its first overtones $\tilde{\nu}_{as_1}$ and $\tilde{\nu}_{as_2}$.

Returning to Fig. 8 we see now that the quasiperiodic spectral pattern in J_0 comprises repeated and interleaved occurrences of spectra corresponding to mesobatic wave-packet trajectories for which $\delta=n\pi$ (nodes) and $(n+1/2)\pi$ (antinodes), respectively. It follows that δ varies continuously with rotational state and that the overall pattern arises through and is a fingerprint of dynamical quantum interference; "dynamical" in the sense that the interference effect rests on synchronization of wave-packet trajectories. From this viewpoint the system can be seen as a quantum matter-wave relative of the pulsed optical Michelson interferometer. Variation of the rotational state would then correspond to a change in the optical path length difference between the two interferometer arms.

D. Spectral signatures of mesobatic wave-packet trajectories

The spectral components of the thermally averaged data, hence, correlate strongly with the distinct features of the bi- and astable types of mesobatic wave-packet motion. In fact, no other significant features were observed, which, at first thought, is a surprising result. The mesobatic conditions demonstratively are sensitive to the rotational state of the system and it has been assumed by us [17] and others [19,20] that summation over rotational states would tend to wash out the quantum interference features and, generally, render dynamical interference contributions difficult to observe. As we saw here, however, in summing over many rotational states the individual phases of the spectral components fluctuate strongly and add to zero for all frequencies except for those belonging to the mesobatic trajectories.

Accordingly, the thermally averaged traces and spectra seem to be dominated by features related to dynamical quantum interference. The relative amplitudes of the as_{0-2} and bs_{b+} peaks, which vary strongly with λ_{pu}, hence, would reflect the overall content of astable and bistable mesobatic motion in the averaged spectrum. We interpret this fact such that changing λ_{pu} amounts to scanning the intramolecular quantum Michelson interferometer to produce "fringes" in the amplitude variation of the two archetypal spectra. Thus, the vanishing intensity observed in the experimental spectra for the bs_{b+} peak at $\lambda_{pu}=895$ nm would correspond to a situation where the quantum phase difference in the forked part of the mesobatic trajectories satisfies $\delta=(n+1/2)\pi$. Scanning to either side of this minimum we tune δ, by the combined action of wave-packet momentum change [15,16,19–22] and relative path length difference [20], and get contributions from the surrounding $\delta=n\pi$ fringes.

We thus can understand also the resonancelike behavior in the pump wavelength dependence of the bs_{b+} peak as arising from dynamical quantum interference, analogous to what is observed for the bound-unbound IBr $(B\,^3\Pi_{0+})$ system [15,16,22]. Moreover, we can appreciate the observed differences between the experiments and the calculations. The quantum phase difference part of the mesobatic conditions, necessarily, is very sensitive to the molecular characteristics, the foremost being potential energy curve topology and particulars of the curve coupling, whereas the timing condition is not so strict. The calculations, accordingly, reproduce qualitatively the mesobatic features. The absolute phase difference δ is with the current precision of theoretical methods difficult to reproduce, however, which accounts for the difficulties of the calculations in reproducing the relative spectral amplitudes.

V. CONCLUSION

Following up on a previous Letter [17], we here continued investigating the quantum wave-packet dynamics in a bound-bound state system exhibiting intermediate coupling strength, the $Rb_2(A\,^1\Sigma_u^+ \sim b\,^3\Pi_u)$ system coupled by spin-orbit interaction.The studies were performed both experimentally by ultrafast pump-probe spectroscopy and theoretically by time-resolved quantum dynamics calculations.

We found that the observed data are dominated by strong dynamical quantum interference. The origin of this interference is similar to that responsible for long-lived resonances in bound-unbound systems and corresponds to strongly entangled diabatic and adiabatic wavepacket motion, here termed mesobatic trajectories. General characteristic features of such trajectories are that on one side of the crossing they have only one branch, i.e., a single turning point, whereas on the other side they divide into both potential curves and that the round-trip time in the two paths is similar.

Depending on the accumulated quantum phase difference δ in the forked part of the trajectory, two classes of mesobatic motion could be discerned, bistable and astable. Bistable motion, which is the kind appearing also in bound-unbound systems, arises if $\delta = n\pi$, irrespective of the nonadiabatic transfer probability at the crossing. The two wave-packet fractions in the forked part of the trajectory then rejoin and go completely into the single branch part of the trajectory from which the wave packet started. If instead $\delta = (n+1/2)\pi$ and the nonadiabatic transfer probability is $1/2$ then the joint wave packet always goes into the alternate single branch path with respect to its origin. This constitutes the astable mesobatic trajectory.

Mesobatic trajectories were observed in the calculations and their characteristic features identified. It was found that by varying the initial rotational state an effect similar to scanning the optical path length difference in a pulsed optical Michelson interferometer was obtained as, effectively, δ was scanned. This effect is observable in the experiments through the pump wavelength dependence of the power spectra of the measured pump-probe delay traces. Thus, on varying this wavelength, large changes in the spectral peak amplitudes were seen and, as for the bound-unbound IBr ($B\,^3\Pi_{0+}$) system [15,16,22], attributed to quantum interference fringes as δ was tuned.

The mesobatic wave-packet motion was for this particular system found to be robust with respect to thermal averaging. We, hence, concluded that the interference features are not generally washed out by averaging over initial quantum states as previously suggested. On the contrary, they are, at least for the case treated here, dominating the thermally averaged signal.

To sum up, we proved the existence of bistable and astable mesobatic wave-packet trajectories in the quantum dynamics of a bound-bound state fully coupled system. The signatures of the corresponding quantum matter-wave interference, moreover, were demonstrated to be easily observable in experiments, which means that thermal averaging did not severely obscure the quantum interference features. On the contrary, the system may be viewed as a quantum relative of a pulsed optical Michelson interferometer and the availability of a multitude of populated initial states facilitates to some extent scanning over wave-packet interference fringes.

ACKNOWLEDGMENTS

We thank Stig Stenholm for discussions on intramolecular wave-packet interference and the authors of Refs. [25,27] for providing their original data files. We are also grateful to Mauritz Andersson for assistance in setting up the calculations. The work was supported by the Swedish Research Council (VR).

[1] A. Friedland, Phys. Rev. D **64**, 013008 (2001).
[2] A. Thiel, J. Phys. G **16**, 867 (1990).
[3] M. Larsson, Annu. Rev. Phys. Chem. **48**, 151 (1997).
[4] S. Hahn and G. Stock, J. Phys. Chem. B **104**, 1146 (2000).
[5] L. D. Landau, Phys. Z. Sowjetunion **2**, 46 (1932).
[6] C. Zener, Proc. R. Soc. London, Ser. A **137**, 696 (1932).
[7] L. J. Butler, Annu. Rev. Phys. Chem. **49**, 125 (1998).
[8] W. Domcke and G. Stock, Adv. Chem. Phys. **100**, 1 (1997).
[9] M. Baer, Phys. Rep. **358**, 75 (2002).
[10] D. R. Yarkony, J. Phys. Chem. A **105**, 6277 (2001).
[11] *Non-adiabatic Effects in Chemical Dynamics*, edited by M. S. Child and M. A. Robb [Faraday Discuss. **127**,1 (2004)].
[12] H. Nakamura, in *Dynamics of Molecules and Chemical Reactions*, edited by R. E. Wyatt and J. Z. H. Zhang (Marcel Dekker, New York, 1996).
[13] M. S. Child, *Semiclassical Mechanics with Molecular Applications* (Oxford Science Publications, Oxford 1991).
[14] W. Qin, D. G. McCoy, L. Torop, and A. J. Blake, Chem. Phys. **221**, 77 (1997).
[15] M. J. J. Vrakking, D. M. Villeneuve, and A. Stolow, J. Chem. Phys. **105**, 5647 (1996).
[16] M. Shapiro, M. J. J. Vrakking, and A. Stolow, J. Chem. Phys. **110**, 2465 (1999).
[17] B. Zhang, N. Gador, and T. Hansson, Phys. Rev. Lett. **91**, 173006 (2003).
[18] A. D. Bandrauk and M. L. Sink, J. Chem. Phys. **74**, 1110 (1981).
[19] H. Kono and Y. Fujimura, Chem. Phys. Lett. **184**, 497 (1991).
[20] H. Dietz and V. Engel, Chem. Phys. Lett. **255**, 258 (1996).
[21] N. Balakrishnan, B. D. Esry, H. R. Sadeghpour, S. T. Cornett, and M. J. Cavagnero, Phys. Rev. A **60**, 1407 (1999).
[22] A. N. Hussain and G. Roberts, J. Chem. Phys. **110**, 2474 (1999).
[23] H. O. Karlsson, Eur. Phys. J. D **11**, 207 (2000).
[24] M. S. Child, Mol. Phys. **32**, 1495 (1976).
[25] D. Edvardsson, S. Lunell, and C. M. Marian, Mol. Phys. **101**, 2381 (2003).
[26] H. Lefebvre-Brion and R. W. Field, *Perturbations in the Spectra of Diatomic Molecules* (Academic, Orlando, FL, 1986).
[27] S. J. Park, S. W. Suh, Y. S. Lee, and G.-H. Jeung, J. Mol. Spectrosc. **207**, 129 (2001).
[28] C. Effantin, O. Babaky, K. Hussein, J. d'Incan, and R. F. Barrow, J. Phys. B **18**, 4077 (1985).
[29] C. Lisdat, O. Dulieu, H. Knöckel, and E. Tiemann, Eur. Phys. J. D **17**, 319 (2001).
[30] M. J. O'Callaghan, A. Gallagher, and T. Holstein, Phys. Rev. A **32**, 2754 (1985).
[31] V. Kokoouline, O. Dulieu, and F. Masnou-Seeuws, Phys. Rev. A **62**, 022504 (2000).
[32] C. Amiot, O. Dulieu, and J. Vergès, Phys. Rev. Lett. **83**, 2316 (1999).
[33] N. Gador, B. Zhang, and T. Hansson (unpublished).
[34] M. D. Feit, J. A. Fleck, and A. Steiger, J. Comput. Phys. **47**, 412 (1982).
[35] M. D. Feit and J. A. Fleck, J. Chem. Phys. **78**, 301 (1983).
[36] L. M. Andersson, H. O. Karlsson, O. Goscinski, L.-E. Berg, M. Beutter, and T. Hansson, Chem. Phys. **241**, 43 (1999).
[37] N. Rosen and C. Zener, Phys. Rev. **40**, 502 (1932).
[38] B. M. Garraway and K.-A. Suominen, Rep. Prog. Phys. **58**, 365 (1995).